

A Semi-Lagrangian Double Fourier Method for the Shallow Water Equations on the Sphere

Anita T. Layton¹

Department of Mathematics, University of North Carolina, Chapel Hill,

North Carolina, U.S.A.

`layton@amath.unc.edu`

William F. Spitz

Sandia National Laboratories, Albuquerque, New Mexico, U.S.A.

`wfspitz@sandia.gov`

Abstract

We describe a numerical method, based on the semi-Lagrangian semi-implicit approach, for solving the shallow water equations (SWEs) in spherical coordinates. The most popular spatial discretization method used in global atmospheric models is currently the spectral transform method, which generates high-order numerical solutions and provides an elegant solution to the pole problems induced by a spherical coordinate system. However, the standard spherical harmonic spectral transform method requires associated Legendre transforms, which for problems with resolu-

tions of current interest, have a computational complexity of $\mathcal{O}(N^3)$, where N is the number of spatial subintervals in one dimension. Thus, the double Fourier spectral method, which uses trigonometric series, may be a viable alternative. The advantage of the double Fourier method is that fast Fourier transforms, which have a computational complexity of $\mathcal{O}(N^2 \log N)$, can be used in both the longitudinal and latitudinal directions. In this implementation, the SWEs are discretized in time by means of the three-time-level semi-Lagrangian semi-implicit method, which integrates along fluid trajectories and allows large time steps while maintaining stability. Numerical results for the standard SWEs test suite are presented to demonstrate the stability and accuracy of the method.

Key words: shallow water equations, double Fourier series, numerical weather prediction, spectral methods, semi-Lagrangian scheme, semi-implicit scheme, spherical coordinates

Subject classifications: 65N35, 76B15, 86A10

1 Introduction

The accuracy of global weather and climate models depends on many factors, including the accuracy of the knowledge of the state of the atmosphere at the initial time, the numerical methods employed, and the resolution. Climate and weather prediction computations are known to be very time-consuming.

¹ Part of this work was done while the author was at the Advanced Study Program, National Center for Atmospheric Research.

In particular, a long-standing problem in the integration of numerical weather prediction models is that with explicit Eulerian time discretization methods the maximum permissible time step is restricted by stability rather than accuracy. That is, in order for the integration to be stable, the time step has to be so small that the time truncation error is much smaller than the spatial truncation error, resulting in high computation cost. Early models used an explicit leapfrog method, in which the time step is limited by both the Courant-Friedrichs-Lewy (CFL) condition as well as the propagation of gravity waves. Discretization schemes based on the semi-Lagrangian treatment of advection offer the promise of larger time steps, with no loss in accuracy compared to Eulerian-based advection schemes [17,21]. Since gravity terms may render the equations stiff and thus severely restrict the time step even with semi-Lagrangian advection approximations, one needs to combine the semi-Lagrangian formulation with semi-implicit time-stepping to obtain maximum benefit from the semi-Lagrangian approach [15,18]. By combining a semi-Lagrangian treatment of advection and a semi-implicit treatment of gravity terms, it is possible to increase the time step substantially while maintaining numerical stability [16,17].

In most global atmospheric applications, spatial discretization schemes are based on the spectral transform method [8,25], in which solution fields are expressed as spherical harmonic expansions. Since the spherical harmonics are the natural representation of a two-dimensional field on the surface of a

sphere, the spectral approach provides an elegant solution to the *pole problem*, including the fact that some variables (e.g., the longitudinal and latitudinal velocity components) may be multi-valued at the poles. Also, since the spherical harmonics are eigenfunctions of the spherical Laplace operator, the resulting semi-implicit Helmholtz problem is trivial to solve. Another advantage of the spectral transform method is that, provided the solution is sufficiently smooth, the method generates numerical approximations with exponential convergence and thus with accuracy higher than most other methods (e.g., finite difference methods) at the same spatial resolution.

Although the spectral transform method seems ideal for the spherical domain, it is computationally expensive, especially at high spatial resolutions, since it requires associated Legendre transforms. In the case of Fourier transforms in the longitudinal direction, fast Fourier Transforms (FFTs) may be used and their computational cost grows as $\mathcal{O}(N^2 \log N)$, where N is the number of subintervals in one spatial dimension. Efficient associated Legendre transforms, analogous to FFTs, have not yet been developed for resolutions of current interest. Therefore, the associated Legendre transforms are often performed by summation and their cost is $\mathcal{O}(N^3)$. Thus there is interest in the atmospheric community in developing alternative numerical methods that have stability and accuracy comparable to that of the spectral transform method but have lower computational cost.

Numerical methods based on Fourier series, rather than spherical harmonics,

have been proposed as a viable alternative to the spectral transform method, in both pseudospectral [11, 20] and spectral [3, 4, 12, 27] forms. Yee solved the Poisson equation by means of a method based on double Fourier series on a spherical surface [27], using sine and cosine series as latitudinal basis functions for odd and even zonal wave numbers, respectively. Cheong applied a modified double Fourier series method to generate solutions of the elliptic and vorticity equations [4] and the shallow water equations (SWEs) [3]. His method is similar to that of Yee [27], but with somewhat different basis functions for even zonal wavenumbers. The advantage of using the double Fourier series is that FFTs can be used in both the longitudinal and latitudinal directions, rather than the associated Legendre transforms used by the spectral transform method in the latitudinal direction, thus resulting in a significant reduction in computational cost. As with the spectral transform method, inversion of the Laplace operator is $\mathcal{O}(N^2)$ for the double Fourier method, making it an attractive candidate for semi-implicit formulations and the resulting Helmholtz equation.

Disadvantages of the double Fourier series are that it permits discontinuities at the poles and the nonlinear terms in the equations give rise to non-isotropic waves which may lead to numerical instability. Both problems can be remedied by applying a spherical harmonic projection [20] (i.e., by performing a least-squares projection of the prognostic variables onto the spherical harmonics) or a diffusive filter [3]. The use of a spherical harmonic projection allows one

to obtain solutions that have the same accuracy of those obtained by means of the spherical harmonic spectral transform method, but has the disadvantage of re-introducing associated Legendre transforms into the dynamics and thus increasing the computational cost.

In this study, we develop a numerical method, based on the three-time-level semi-Lagrangian semi-implicit (SLSI) method and the double Fourier series, for obtaining solutions of the SWEs in spherical coordinates. Because the nonlinearity in the SWEs arises mostly from the advection terms, it has been conjectured that by incorporating the advection terms in the Lagrangian derivatives, one may obtain a numerical method that is stable, yields the same solutions as the spectral transform method within round-off errors, and does not require associated Legendre transforms. We tested this conjecture and our results indicate that a weak nonlinearity still persists in the scalar components of the motion equations and in the quadratic term in the continuity equation (or, alternatively, in the logarithmic term if the logarithmic formulation of the continuity equation is used). We demonstrate, unfortunately, that this nonlinearity necessitates the use of some type of post-processing on the prognostic variables, such as the spectral harmonic projection.

In Section 2, we describe how the SWEs are discretized in time using the three-level SLSI method and in space using the double Fourier method. In Section 3, we present convergence results for the method using the standard test suite for the SWEs in spherical geometry [24]; we show that the method

generates third-order accurate solutions and that the method is stable with CFL number greater than 1. We also compare the efficiency of the model to one that uses the logarithmic form of the continuity equation as in [5].

2 The Semi-Lagrangian Double Fourier Method

Because the earth is approximately spherical, most global atmospheric models in use today are based on spherical coordinates. To define the SWEs on the sphere, let $0 \leq \lambda < 2\pi$ be longitude and $0 \leq \theta \leq \pi$ be colatitude; let \vec{v} denote the vector (u, v) , where u and v are the wind velocity components in the longitudinal and colatitudinal directions, respectively; ϕ' be the geopotential perturbation from the mean geopotential ϕ^* , which is assumed to be constant; a be the radius of the earth; Ω be its rotational speed; and $f \equiv 2\Omega \sin \theta$ be the Coriolis parameter. Since u and v are multi-valued at the poles, we adopt the approach of Côté and Staniforth [6] and compute the components of the wind images instead: $U \equiv u \sin \theta$ and $V \equiv v \sin \theta$. Using this notation, the vector form of the SWEs in spherical coordinates is given by

$$\sin \theta \frac{d\vec{v}}{dt} + f \sin \theta \hat{k} \times \vec{v} + \sin \theta \vec{\nabla} \phi = 0, \quad (1)$$

$$\frac{d\phi'}{dt} + (\phi' + \phi^*) \vec{\nabla} D = 0, \quad (2)$$

where \hat{k} is the outward radial unit vector, the divergence $D \equiv \vec{\nabla} \cdot \vec{v}$, and

$$\frac{d}{dt} \equiv \frac{\partial}{\partial t} + (\vec{v} \cdot \vec{\nabla}), \quad \vec{\nabla} \equiv \frac{\hat{i}}{a \cos \theta} \frac{\partial}{\partial \lambda} + \frac{\hat{j}}{a} \frac{\partial}{\partial \theta}. \quad (3)$$

Note that (1) differs from the standard form in that it is scaled by $\sin \theta$. This prevents $\sin \theta$ from appearing in the denominator of any term and facilitates the use of standard trigonometric identities in the double Fourier spectral method.

2.1 The three-level semi-Lagrangian semi-implicit method

Generally, a two-level semi-Lagrangian semi-implicit method is preferred to a three-level method. In [5] Cote and Staniforth developed a method based on the two-time-level SLSI method and the spherical harmonic spectral transform method, and showed that their method is twice as efficient as a similar method based on the three-time-level SLSI method. However, an analogous development for the double Fourier expansion is not as efficient. See Appendix A for details. For this reason we pursue the three-time-level approach.

A semi-Lagrangian time discretization scheme in spherical coordinates approximates the Lagrangian derivative along particle trajectories defined by the velocity vector with components $d\lambda/dt = u/(a \cos \theta)$ and $d\theta/dt = v/a$. In the numerical discretization, let Δt denote the time step and let $t_n \equiv n\Delta t$ be the n -th time-level for $n = 0, 1, 2, \dots$. Let $(\delta\lambda^{n+1}, \delta\theta^{n+1})$ be the displacement of a fluid particle in the time interval t_{n-1} to t_{n+1} , ending at the downstream point (λ, θ) at t_{n+1} . We adopt the three-time-level scheme which approximates a function on a trajectory originating at the upstream point $(\lambda - \delta\lambda^{n+1}, \theta - \delta\theta^{n+1})$

and terminating at (λ, θ) . For an arbitrary function $\psi(\lambda, \theta, t)$, let $\tilde{\psi}^{n-1}$ be the upstream function for the time interval t_{n-1} to t_{n+1} . That is, for the downstream grid point (λ, θ) associated with the displacement $(\delta\lambda^{n+1}, \delta\theta^{n+1})$,

$$\tilde{\psi}^{n-1}(\lambda, \theta) \equiv \psi(\lambda - \delta\lambda^{n+1}, \theta - \delta\theta^{n+1}, t_{n-1}). \quad (4)$$

The Lagrangian derivative in the interval t_{n-1} to t_{n+1} is approximated by

$$\left(\frac{\widetilde{d\psi}}{dt}\right)^n \approx \frac{\psi^{n+1} - \tilde{\psi}^{n-1}}{2\Delta t}. \quad (5)$$

The semi-Lagrangian approach provides stable approximations for advection with virtually no time-step restriction. However, if the gravity terms are treated explicitly, they will severely restrict the time step even when semi-Lagrangian advection approximations are used. Therefore, to obtain maximum benefit from the semi-Lagrangian approach, we combine the semi-Lagrangian approximations with semi-implicit approximations. A semi-implicit treatment of the gravity terms implies that a function is averaged in time along particle trajectories:

$$\tilde{\psi}^n \approx \frac{\psi^{n+1} + \tilde{\psi}^{n-1}}{2}. \quad (6)$$

To discretize (1) and (2) using the three-time-level SLSI scheme, we first compute the trajectories (i.e., $\delta\lambda^{n+1}$ and $\delta\theta^{n+1}$) in three-dimensional Cartesian geometry with the restriction that the trajectories are confined on the surface of a sphere [5]. The momentum equation (1) is discretized in time in its vector form to avoid instability associated with the metric term $(U^2 + V^2) \cot \theta$, which ap-

pears in the latitudinal component of (1) [13]. We follow Ritchie's approach [13] and discretize (1) in tangential Cartesian coordinates. We let $(\hat{\lambda}^-, \hat{\theta}^-)$, $(\hat{\lambda}^0, \hat{\theta}^0)$, and $(\hat{\lambda}^+, \hat{\theta}^+)$ denote unit vectors associated with the upstream, midpoint, and downstream position vectors, respectively. The upstream and midpoint vectors vary every time level, but for notational simplicity we have omitted the time dependence. To derive the transformation to the tangential Cartesian plane from horizontal vectors on a trajectory, we let $(\hat{\lambda}^0, \hat{\theta}^0)$ be the unit vector of the tangential Cartesian plane. Using this notation, a SLSI time discretization of the horizontal momentum equation (1) is given by

$$\sin \theta \left(\frac{\vec{v}^{n+1} - \vec{v}^{n-1}}{2\Delta t} \right) + \sin \theta \left(\frac{\vec{\nabla} \phi'^{n+1} + \vec{\nabla} \tilde{\phi}'^{n-1}}{2} \right) = -(\widetilde{f \sin \theta \hat{k}} \times \vec{v})^n, \quad (7)$$

which can be rewritten in terms of the wind images

$$\begin{aligned} & \left(U^{n+1} + \frac{\Delta t}{a} \frac{\partial \phi'^{n+1}}{\partial \lambda} \right) \hat{\lambda}^+ + \left(V^{n+1} + \frac{\Delta t}{a} \sin \theta \frac{\partial \phi'^{n+1}}{\partial \theta} \right) \hat{\theta}^+ \\ & = (\widetilde{\sin \theta p_\lambda})^{n-1} \hat{\lambda}^- + (\widetilde{\sin \theta p_\theta})^{n-1} \hat{\theta}^- - 2\Delta t \tilde{f}^n (-\tilde{V}^n \hat{\lambda}^0 + \tilde{U}^n \hat{\theta}^0), \end{aligned} \quad (8)$$

where

$$p_\lambda = u - \frac{\Delta t}{a \sin \theta} \frac{\partial \phi'}{\partial \lambda}, \quad p_\theta = u - \frac{\Delta t}{a} \frac{\partial \phi'}{\partial \theta}. \quad (9)$$

The vector equation (8) is then expressed in terms of the $\hat{\lambda}^0$ and $\hat{\theta}^0$ components. To this end, the unit vectors $(\hat{\lambda}^-, \hat{\theta}^-)$ and $(\hat{\lambda}^+, \hat{\theta}^+)$ are related to the

mid-trajectory unit vectors $(\hat{\lambda}^0, \hat{\theta}^0)$ as follows

$$\hat{\lambda}^\pm = \frac{Y^\pm \hat{\lambda}^0 + X^\pm \hat{\theta}^0}{\sqrt{(X^\pm)^2 + (Y^\pm)^2}}, \quad (10)$$

$$\hat{\theta}^\pm = \frac{Y^\pm \hat{\theta}^0 - X^\pm \hat{\lambda}^0}{\sqrt{(X^\pm)^2 + (Y^\pm)^2}}, \quad (11)$$

$$X^\pm \equiv \cos \Theta \sin \gamma^\pm \cos \tilde{\theta}^n + (1 - \sin \Theta) \cos \gamma^\pm \sin \gamma^\pm \sin \tilde{\theta}^n, \quad (12)$$

$$Y^\pm \equiv \sin \tilde{\theta}^n - \cos \Theta \sin \gamma^\pm \cos \tilde{\theta}^n - (1 - \sin \Theta) \cos^2 \gamma^\pm \sin \tilde{\theta}^n, \quad (13)$$

where $\tilde{\theta}^n$ is the colatitudinal coordinate of the midpoint position,

$$\Theta \equiv \frac{\Delta t}{a} \sqrt{(\tilde{u}^n)^2 + (\tilde{v}^n)^2}$$

is the angular displacement from the upstream position to the midpoint position (or, alternatively, from the midpoint position to the downstream position), and $\gamma^\pm \equiv \tan^{-1}(\pm \tilde{v}^n / \pm \tilde{u}^n)$. By substituting (10)–(13) into (8) and separating the components of $\hat{\lambda}^0$ and $\hat{\theta}^0$, we obtain

$$U^{n+1} + \frac{\Delta t}{a} \frac{\partial \phi'^{n+1}}{\partial \lambda} = X^+ q_2 + Y^+ q_1 \equiv Q_1, \quad (14)$$

$$V^{n+1} + \frac{\Delta t}{a} \sin \theta \frac{\partial \phi'^{n+1}}{\partial \theta} = Y^+ q_2 - X^+ q_1 \equiv Q_2, \quad (15)$$

where

$$q_1 \equiv \frac{Y^- \tilde{p}_\lambda^{n-1} - X^- \tilde{p}_\theta^{n-1}}{\sqrt{(X^-)^2 + (Y^-)^2}} + 2\Delta t \tilde{f}^n \tilde{v}^n, \quad (16)$$

$$q_2 \equiv \frac{X^- \tilde{p}_\lambda^{n-1} + Y^- \tilde{p}_\theta^{n-1}}{\sqrt{(X^-)^2 + (Y^-)^2}} - 2\Delta t \tilde{f}^n \tilde{u}^n. \quad (17)$$

The time-discretized form of the continuity equation (2) is

$$\phi^{m+1} + \Delta t \phi^* D^{n+1} = \tilde{\phi}^{n-1} - \Delta t \phi^* \tilde{D}^{n-1} - 2\Delta t \tilde{\phi}^n \tilde{D}^n \equiv Q_3. \quad (18)$$

The departure points usually fall between grid points and spatial interpolation is required to obtain function values at departure points. Cubic polynomial interpolation gives fourth-order spatial truncation errors with very little damping [2], and is thus the method of choice in our implementation. To avoid the decoupling of solutions computed at odd and even time-levels, a Robert filter [1,14] is applied to the prognostic variables at the end of every time step.

2.2 The double Fourier method

To solve (14)–(18), we first cross-differentiate (14) and (15) to yield

$$\zeta^{n+1} \sin^2 \theta = \frac{1}{a} \left(-\sin \theta \frac{\partial}{\partial \theta} Q_1 + \frac{\partial}{\partial \lambda} Q_2 \right) \equiv L, \quad (19)$$

$$D^{n+1} \sin^2 \theta + \Delta t \sin^2 \theta \nabla^2 \phi^{m+1} = \frac{1}{a} \left(\frac{\partial}{\partial \lambda} Q_1 + \sin \theta \frac{\partial}{\partial \theta} Q_2 \right) \equiv M, \quad (20)$$

where the vorticity ζ and the divergence D are related to the wind images U and V through the stream function ψ and the velocity potential χ :

$$U = \frac{1}{a} \frac{\partial \chi}{\partial \lambda} - \frac{\sin \theta}{a} \frac{\partial \psi}{\partial \theta}, \quad V = \frac{1}{a} \frac{\partial \psi}{\partial \lambda} + \frac{\sin \theta}{a} \frac{\partial \chi}{\partial \theta}, \quad (21)$$

$$\sin^2 \theta \nabla^2 \psi = \zeta \sin^2 \theta, \quad \sin^2 \theta \nabla^2 \chi = D \sin^2 \theta. \quad (22)$$

To solve (18)–(20), we eliminate the divergence D^{n+1} to yield the Helmholtz

equation

$$\sin^2 \theta \left(1 - \Delta t^2 \nabla^2\right) \phi^{n+1} = \sin^2 \theta Q_3 - \Delta t M. \quad (23)$$

We then spatially discretize (19)–(23) by expressing all the scalar functions as double Fourier expansions. To this end, let $\xi(\lambda, \theta)$ be an arbitrary scalar function on the sphere. Then,

$$\xi(\lambda, \theta) = \sum_{m=-N}^N \xi_m(\theta) e^{im\lambda}, \quad (24)$$

where the single Fourier expansion $\xi_m(\theta)$ is given by

$$\xi_m(\theta) = \begin{cases} \sum_{\ell=0}^N \xi_{m,\ell} \cos \ell\theta, & m \text{ even,} \\ \sum_{\ell=0}^N \xi_{m,\ell} \sin \ell\theta, & m \text{ odd,} \end{cases} \quad (25)$$

where m is the longitudinal (or zonal) wave number, ℓ is the latitudinal (or meridional) wave number, and $i \equiv \sqrt{-1}$. The expansion (24)–(25) was first proposed by Yee [26], based on the ideas of Orszag [12].

It can be shown [27] that the matrix arising from the discretization of the Helmholtz equation (23) is tridiagonal. Thus, solution of (23) for ϕ^{n+1} requires $\mathcal{O}(N^2)$ operations.

The following algorithm advances the solution by one time step:

- (1) In grid space, compute fluid trajectories by estimating $\delta\lambda^{n+1}$ and $\delta\theta^{n+1}$.
- (2) Using cubic Lagrange interpolations, compute upstream values for q_1 , q_2 , and Q_3 using (16)–(18).

- (3) Form Q_1 and Q_2 in grid space using (14) and (15). Then transform Q_1 , Q_2 , and Q_3 from grid space to spectral space.
- (4) In spectral space, compute L and M from Q_1 and Q_2 using (19) and (20).
- (5) In spectral space, solve the Helmholtz equation (23) for ϕ^{m+1} . Then use ϕ^{m+1} and (20) to compute D^{n+1} . Solve (19) for ζ^{n+1} .
- (6) Apply the spherical harmonic projection to the prognostic variables ϕ^{m+1} , ζ^{n+1} , and D^{n+1} .
- (7) Update U^{n+1} and V^{n+1} using ζ^{n+1} , D^{n+1} , and equations (21) and (22).
- (8) Using (9), compute p_λ and p_θ from U^{n+1} , V^{n+1} , and ϕ^{m+1} in spectral space.
- (9) Transform U^{n+1} , V^{n+1} , ϕ^{m+1} , p_λ and p_θ from spectral space to grid space.

Transforming a variable between spectral space and grid space introduces a data transposition in a parallel implementation. Thus, a parallel implementation of the SLSI double Fourier method involves eight transposes for each time step: three backward transforms in step (3) and five forward transforms in step (9).

2.3 Spectral filtering

To prevent aliasing that arises from the quadratic term in the continuity equation (2), the quadratic truncation grid (i.e., the 2/3-truncation rule) is used. Since the linear truncation grid yields more accurate spectral approximations

than the quadratic grid for the same resolution, in Section 3.3 we study the efficiency of the SLSI double Fourier method when a linear grid is used in conjunction with a weakly-nonlinear logarithmic form of the continuity equation, which does not contain a quadratic term. For most spectral methods (e.g., [5]), a linear truncation grid corresponds to one for which all of the representable waves are retained. In contrast, in our implementation of the double Fourier method, the $\sin^2 \theta$ operations expand the wave spectrum by two and give rise to aliasing. Thus, in order to maintain stability, the two waves with the highest wave numbers must be truncated at each time step.

The expansion (24)–(25) permits discontinuities at the poles and nonisotropic waves, which may lead to a prohibitive time-step restriction and numerical instability. To avoid these problems, we apply the spherical harmonic projection [20] to the prognostic variables (ϕ' , ζ , and D) at the end of every time step. The spherical harmonic projection is obtained by projecting the single Fourier data onto the space of spherical harmonics. This is equivalent to truncating certain waves such that the retained waves are isotropic on the surface of a sphere. The spherical harmonic projection re-introduces associated Legendre transforms into the computations, but the resulting method is still faster than the standard spectral transform method because harmonic transforms are limited to the projection and are not used to compute spatial derivatives [19]. Moreover, by using the spherical harmonic projection, our method produces exactly the same results as the equispaced spectral transform method to within

roundoff error.

Projecting each of the prognostic variables involves two associated Legendre transforms, thus a total of six transforms are required for each time step. Compared to the eight transforms required for the most efficient semi-Lagrangian spectral transform method [13] or an average of 13 transforms for most forms of the Eulerian spectral transform methods [22], our approach offers reductions of 25%–54% in the number of associated Legendre transforms required. We implemented the spherical harmonic projection using the associated Legendre projection developed by Spatz and Swarztrauber [19], based on the weighted orthogonal complement to the associated Legendre functions. Compared to the standard approach, this approach provides a 12.5% reduction in operation count for a quadratic truncation grid and reduces the memory storage from $\mathcal{O}(N^3)$ to $\mathcal{O}(N^2)$ without requiring re-computation of associated Legendre functions [19].

2.4 Spatial convergence properties of the method

When combined with an Eulerian time discretization, the double Fourier method, like the spectral transform method, generates numerical approximations with exponential convergence [3]. However, when a semi-Lagrangian time discretization is used, upstream function values are required. These upstream values could be computed from the spectral representation of the

functions, which would give highly accurate approximations. Unfortunately, these computations are $\mathcal{O}(N^4)$ and the resulting implementation would be prohibitively expensive. Thus, in our implementation, cubic Lagrange interpolations are used to estimate upstream function values. The truncation error associated with cubic Lagrange interpolation is fourth order; thus, one might expect the SLSI double Fourier method to generate fourth-order approximations. However, the solutions reported in Section 3 exhibit third-order convergence in space. We attribute this sub-optimal convergence (i.e., a convergence that is slower than that of the spatial interpolation method) to the $[(X^-)^2 + (Y^-)^2]^{-1/2}$ factor in Q_1 and Q_2 in (14)–(17). Since

$$\sqrt{(X^-)^2 + (Y^-)^2} = \cos \tilde{\theta},$$

we have $[(X^-)^2 + (Y^-)^2]^{-1/2} \rightarrow \mathcal{O}(1/\Delta\theta)$ as $\theta \rightarrow \pm\pi/2$, thus giving rise to larger truncation errors and reducing the order of convergence by one near the poles. As the simulation progresses, these larger polar errors propagate over the sphere and eventually contaminate the rest of the solution. This phenomenon has been reported elsewhere [10, 23].

3 Numerical Results

We tested the SLSI double Fourier method using the complete Williamson *et al.* test suite for the SWEs in spherical geometry [24]. In this section, we first present spatial convergence results and show that the method generates stable

and convergent solutions for all test cases. Then we demonstrate that, owing to its Lagrangian nature, the method is stable with a CFL number $\gg 1$. Finally, we investigate the efficiency of the method when a linear truncation grid is used in conjunction with the logarithmic form of the continuity equation as in [5].

All computations reported below were performed using Fortran programs in double precision on a Sun 6500 server with an Ultra-2 400 MHz processor and 24 GB of RAM.

3.1 Convergence results for standard test cases

Test cases 1–4

Analytic solutions exist for test cases 1–4; high-resolution numerical reference solutions [9] are provided for the remaining test cases 5–7. Test case 1 describes the linear advection of a cosine bell over the pole and tests the advective component of the numerical method in isolation. A cosine bell of height 1000m is advected once around the sphere; the divergence is chosen to be zero for this test case. The rotation of the earth is allowed to have an angle α from the coordinate axes to test the capability of the numerical method to handle the pole problem. Thus, by choosing different α 's, different orientations of the advecting wind can be simulated, including advection around the equator ($\alpha = 0$), directly over the poles ($\alpha = \pi/2$), and minor shifts from these two

orientations ($\alpha = 0.05$ and $\pi/2 - 0.05$). Figures 1 and 2 show contour plots of the solution and errors for the geopotential after 12 days, during which the cosine bell was advected once around the sphere and directly over the poles. A spatial grid of T85 was used. The maximum and minimum values of the geopotential approximation are 979.5m and -4.3m, respectively, and the maximum geopotential error is 20.5m. Thus, the solution translated with little change in shape. However, because of the discontinuous second derivatives in the initial data, results for case 1 show only approximately first-order convergence in space, instead of third-order convergence.

Test case 2 is a steady-state solution to the nonlinear SWEs. It consists of solid body rotation or zonal flow with the corresponding geostrophic height field. In our simulations, a time step of $\Delta t = 15$ min was used. Table 1 shows normalized l_2 errors in ϕ after 5 days for $\alpha = \pi/2$, where α is the angle between the computational pole and the axis of the solid body rotation, for different spatial resolutions. The results indicate third-order convergence in space, which is the convergence rate we expect as explained in Section 2.4. Similar results were obtained for $\alpha = 0.0, 0.05, \pi/2 - 0.05$ (not shown).

Test case 3 is similar to test case 2 except that the wind field is nonzero in a limited region. As a result, if the model resolution is low, the initial field may not be expressed accurately. As in case 2, a time step of $\Delta t = 15$ min was used. In Table 1 normalized l_2 errors and spatial convergence in ϕ for $\alpha = \pi/3$ for a 5-day simulation are computed. The results are consistent with the expected

third-order convergence. Similar results were obtained for $\alpha = 0$ (not shown).

In test case 4 forcing terms are added to the right sides of (1)–(2) and chosen such that analytic solutions are known a priori for the resulting nonlinear unsteady equations. A small time step of $\Delta t = 5$ min was used to ensure that the temporal error was small compared to the spatial error. Table 1 shows normalized l_2 errors in ϕ after 5 days for successively refined spatial grids. The numerical solutions converge in space at a rate of approximately third order, although the convergence slows down at high spatial resolutions when the temporal error is no longer negligible.

Test cases 5–7

Because no known analytic solution exists for test cases 5–7, we compare our results to highly refined spectral transform solutions [9]. As in the reference solution, explicit diffusion is used to maintain stability for these cases. At each time step, we apply the following scale-dependent and resolution-dependent filter to the prognostic variables

$$\xi^n \leftarrow \xi^n - c\Delta\lambda^3\nabla^4\xi^n, \quad (26)$$

where $\xi = \phi, \zeta, \text{ or } D$, and $c = 10^{-4}a^4$. By scaling the diffusion term by $\Delta\lambda^3$, we ensure that the discrepancy introduced by the explicit diffusion to the numerical solution is of the same order as the spatial truncation error and thus does not affect the spatial convergence rate.

Test case 5 consists of zonal flow as in case 2, with $\alpha = 0$, impinging on a conical mountain, located at (90°W, 30°N). A time step of $\Delta t = 15$ min was used. Figure 3 shows the evolution of normalized l_2 error in ϕ , computed on successively refined spatial resolutions, for 15 days. The numerical solutions are stable but the error fails to converge to zero for two reasons. First, the zonal flow initial conditions and the topography are not in geostrophic balance. Thus, gravity waves of significant magnitude are generated, which in turn are poorly resolved by the semi-implicit reference solution, resulting in an uncertainty of approximately 10^{-3} in the normalized l_2 geopotential error. Moreover, the orography has a discontinuous first derivative and thus violates the smoothness assumption in both the double Fourier expansion and the cubic Lagrangian interpolation. Despite these difficulties, our method, coupled with artificial diffusion, was stable and produced convergent approximations. Indeed, for a resolution higher than T42, the normalized geopotential error remains approximately 10^{-3} for 15 days.

Test case 6 is the stable Rossby-Haurwitz wave with zonal wave number 4. A time step of $\Delta t = 15$ min was used. In the absence of divergence effect, the Rossby-Haurwitz wave should translate zonally with no change in shape [7]. Figure 4 shows the evolution of normalized l_2 error in ϕ , computed on successively refined spatial resolutions, for 14 days. In all our simulations, the initial shape of the wave was preserved.

Test case 7 consists of atmospheric initial conditions of the 500 mb height

and winds from several atmospheric states. The evolution of normalized l_2 geopotential errors for 5 days corresponding to three different sets of initial conditions are shown in Fig. 5. Sub-case (a) is for 0000 GMT December 21, 1978, with strong flow over the north pole; sub-case (b) is 0000 GMT January 16, 1979, characterized initially by two cutoff lows, which develop into a typical block situation; sub-case (c) is 0000 GMT January 9, 1979, which initially has strong zonal flow. A time step of $\Delta t = 15$ min was used in the simulations. The lack of smoothness in the solution results in a lower-than-expected (approximately linear or super-linear) rate of convergence for the method.

3.2 Stability results with large time steps

The semi-Lagrangian scheme offers the advantage of maintaining numerical stability while allowing large time steps with CFL numbers greater than 1. In the following numerical tests, we evaluate the stability of our method using test cases 3, 4, and 7 with large time steps of $\Delta t = 30$ min, 1 hour, and 2 hours. A spatial grid of T85 was used. The normalized l_2 errors in ϕ after 5 days are shown in Table 2. The method was unstable with $\Delta t \geq 3$ hours for test cases 3 and 4, and with $\Delta t \geq 2$ hours for test case 7. The results show that our method allows large time steps with a CFL number substantially larger than 1 (as large as 30.4 for test cases 3 and 4, and as large as 15.2 for test case 7) while maintaining stability. When a sufficiently large time step is used (e.g., $\Delta t \geq 1$ hour for test case 4) such that the temporal truncation

error dominates the spatial truncation error, the numerical solution shows second-order convergence in time.

3.3 Quadratic versus linear truncations

In [5] Côté and Staniforth presented a solution for the SWEs in spherical coordinates by combining the two-time-level SLSI scheme and the spectral transform method. In their model, the nonlinearity in the continuity equation (2) is captured in a logarithmic term as follows:

$$\frac{d}{dt} \log \left(1 + \frac{\phi'}{\phi^*} \right) + D = 0. \quad (27)$$

Because the logarithmic term is linear to the order $(\phi'/\phi^*)^2$, it is only weakly nonlinear. Côté and Staniforth showed that when a “reduced-resolution Gaussian grid” (i.e., a linear truncation grid that retains the same number of waves as a given quadratic truncation grid) was used, their model produced forecasts comparable to those obtained using the higher-resolution grid with quadratic truncation. In this subsection, we compare the stability, accuracy, and efficiency of the logarithmic formulation to the model described in Section 2, which we refer to as the quadratic formulation owing to the quadratic term in the continuity equation.

The logarithmic formulation gives rise to a nonlinear Helmholtz equation, which is solved iteratively. After time-discretizing (27) using the three-time-

level SLSI method, one obtains

$$\log\left(1 + \frac{\phi'^{n+1}}{\phi^*}\right) + \Delta t D^{n+1} = \log\left(1 + \frac{\tilde{\phi}'^{n-1}}{\phi^*}\right) - \Delta t \tilde{D}^{n-1} \equiv Q_3^l. \quad (28)$$

Then the divergence D^{n+1} is eliminated from (28) using (20) to yield the nonlinear Helmholtz equation

$$\left(\sin^2 \theta \log\left(1 + \frac{\phi'^{n+1}}{\phi^*}\right) - \Delta t^2 \sin^2 \theta \nabla^2 \phi'^{n+1}\right) = \sin^2 \theta Q_3^l - \Delta t M, \quad (29)$$

which is solved by means of fixed-point iterations as described in [5]. In our implementation, five fixed-point iterations are used.

Test case 3 is used in the numerical tests. Our choice of test case was motivated by the existence of analytic solution for test case 3 (unlike test cases 5–7), by the full spectrum of its solution (i.e., all waves are excited, unlike test case 2), and by the absence of forcing terms (unlike test case 4). Four models are considered—the logarithmic formulation on linear and quadratic truncation grids, and the quadratic formulation on quadratic truncation grid and on a grid using the 1/2-truncation rule. (Recall that in our implementation of the linear grid, the two waves with the highest wave numbers are truncated at each time step.)

One might suggest that because the nonlinearity in the logarithmic form of the continuity equation (28) is much weaker than in the quadratic form (2), the double Fourier method may be stable without the spherical harmonic projection. However, our results show that weak nonlinearity that still persists

in the scalar components of the motion equations and in the $\log(\phi)$ term of the continuity equation necessitates the use of the spherical harmonic projection to maintain numerical stability.

Simulations were run using a time step of $\Delta t = 15$ min for 5 days. All four models (when coupled with the spherical harmonic projection) were stable and the approximations show third-order convergence. In general, compared to a quadratic truncation grid, a linear truncation grid with the same number of grid points gives more accurate double Fourier approximations of smooth functions by retaining more waves. However, as shown in Table 3, the numerical solutions computed using the logarithmic formulation on a linear grid are slightly less accurate than those computed using the quadratic formulation on a quadratic grid. We attribute this apparent paradox to the interpolation errors. The spatial truncation errors in a numerical solution computed using a SLSI double Fourier method arise from the truncated double Fourier representation and from cubic Lagrange interpolations used in the approximation of upstream function values. The interpolation error is fourth order (third order on a sphere) and thus dominates the double Fourier error, which has exponential convergence.

We tested this hypothesis by first considering the accuracy of the two formulations discretized on grids that truncate more waves than are required to avoid aliasing. When a quadratic truncation grid is used instead of a linear grid, the normalized l_2 geopotential errors in the approximation computed using

the logarithmic formulation increase only by $\sim 1.3\%$ and $\sim 0.4\%$ for $N_\lambda = 128$ and 256, respectively, where N_λ denotes the number of grid points along the longitude; and when a 1/2-truncation is used instead of the 2/3-truncation, which implies that only 9/16 of the waves in the quadratic grid is retained, the normalized l_2 errors in the geopotential computed using the quadratic formulation increase only by $\sim 2.7\%$ and $\sim 0.9\%$ for $N_\lambda = 128$ and 256, respectively. Thus, these results indicate that retaining fewer waves does not significantly reduce the accuracy of the numerical solutions.

We then considered the accuracy of the numerical solutions obtained using fifth-order quartic Lagrange interpolations to approximate upstream function values. The normalized l_2 geopotential errors for the logarithmic formulation are found to be 4.728×10^{-5} and 2.957×10^{-6} for $N_\lambda = 128$ and 256, respectively. And for the quadratic formulation, the normalized l_2 geopotential errors are 4.102×10^{-5} and 2.574×10^{-6} for $N_\lambda = 128$ and 256, respectively. These errors are approximately an order of magnitude smaller than those obtained using cubic Lagrange interpolations. Thus, increasing the accuracy of the spatial interpolations significantly increases the accuracy of the numerical solutions, at the cost of increased computational time and, in a domain decomposed parallel implementation, communication time.

Also present in the numerical solutions computed using the logarithmic formulation (but not the quadratic formulation) are the errors introduced by the iterative solver. When five iterations are used, the residuals are several

orders of magnitude ($\sim 3-5$) smaller than the final normalized l_2 geopotential errors. We also tested the significance of this error by using 10 (instead of 5) fixed-point iterations; the resulting approximations do not show any noticeable increase in accuracy. Because the logarithmic formulation requires the solution of a nonlinear kernel, and thus higher computational costs, and does not give more accurate approximations, we conclude that it is less efficient than the quadratic formulation. Note, however, that the logarithmic formulation is often used in two-time-level SLSI methods (e.g., [5]) because the geopotential-divergence product is unknown at mid-time-level.

4 Discussion

The numerical results presented in Section 3 demonstrate the stability and accuracy of the SLSI double Fourier method. The Lagrangian nature of the method maintains numerical stability while allowing time steps up to ~ 30 times larger than the maximum time step permissible in an Eulerian-based method. Provided that the solution is sufficiently smooth, the method generates approximations with third-order accuracy. Because the double Fourier expansion permits discontinuities at the poles and nonisotropic waves, the spherical harmonic projection [20] is used; that is, the prognostic variables are projected onto the spherical harmonic space at the end of every time step. Aliasing is controlled by means of a quadratic truncation grid. The as-

sociated Legendre transforms required in the spherical harmonic projections unfortunately increases the computational complexity of the method from $\mathcal{O}(N^2 \log N)$ to $\mathcal{O}(N^3)$. Nonetheless, a total of six associated Legendre transforms are required for each time step, which still offers a speedup of 25% compared to the eight associated Legendre transforms required for the most efficient implementation of the semi-Lagrangian spectral transform method. An alternative to the spherical harmonic projection is a diffusive filter such as [3], which is significantly less expensive than the spherical harmonic projection and does not increase the computational complexity of the method. In this study, however, we have chosen to adopt the spherical harmonic projection because it allows the double Fourier method to generate the same approximations as the spectral transform method. In practice however, an implicit diffusive filter would be attractive because of the expense, as long as the resulting errors are guaranteed to be less than the interpolation error, as with the explicit artificial diffusion introduced for cases 5–7.

A Two Time Level Scheme

In a three-time-level scheme, the Coriolis terms in the motion equations (1) are evaluated explicitly at trajectory midpoints at t_n ; in a two-time-level scheme, the Coriolis terms may be averaged along fluid trajectories. Côté and Staniforth [5] describe such a two time-level semi-Lagrangian semi-implicit scheme

for spherical harmonic spectral models. Letting $\zeta_m = [\zeta_{m,m}\zeta_{m,m+1}\cdots\zeta_{m,N-1}]^T$, etc., they developed a linear system for each zonal wave number m ,

$$\mathbf{A}_m\zeta_m + \mathbf{B}_m\delta_m = \mathbf{L}_m, \quad (\text{A.1})$$

$$-\mathbf{B}_m\zeta_m + \mathbf{A}_m\delta_m + \mathbf{C}_m\phi'_m = \mathbf{M}_m, \quad (\text{A.2})$$

$$\tilde{a}\delta_m + \phi'_m = \mathbf{Q}_m. \quad (\text{A.3})$$

For a spherical harmonic expansion, \mathbf{A}_m and \mathbf{C}_m are diagonal and \mathbf{B}_m is tridiagonal. \mathbf{A}_m is, in fact, the discrete Laplace operator for zonal wave number m . For the double Fourier expansion, \mathbf{A}_m and \mathbf{C}_m are tridiagonal.

The vorticity and geopotential can be eliminated from (A.1)–(A.3) to yield the system

$$\zeta_m = \mathbf{A}_m^{-1}(\mathbf{L}_m - \mathbf{B}_m\delta_m), \quad (\text{A.4})$$

$$\phi'_m = \mathbf{Q}_m - \tilde{a}\delta_m, \quad (\text{A.5})$$

$$[\mathbf{A}_m - \tilde{a}\mathbf{C}_m + \mathbf{B}_m\mathbf{A}_m^{-1}\mathbf{B}_m]\delta_m = \mathbf{M}_m - \mathbf{C}_m\mathbf{Q}_m + \mathbf{B}_m\mathbf{A}_m^{-1}\mathbf{L}_m. \quad (\text{A.6})$$

In theory, equation (A.6) can be solved for δ_m , which can then be used to form the right hand sides of equations (A.4)–(A.5). When spherical harmonics are used, the matrix on the left hand side of (A.6) is trivial to compute because \mathbf{A}_m is diagonal. However, for the double Fourier expansion, the tridiagonal \mathbf{A}_m becomes a full matrix when it is inverted, resulting in a full $(N-m) \times (N-m)$ matrix on the left hand side of (A.6). Thus with a double Fourier expansion, solving (A.4)–(A.6) for all m becomes an $\mathcal{O}(N^3)$ algorithm.

Alternatively, an iterative solver may be used and the resulting computations may be $\mathcal{O}(N^2)$, provided that the number of iterations required for conver-

gence is independent of the spatial resolution. Nonetheless, the double Fourier equivalent of [5] appears to present a number of computational challenges. An alternative to [5] is to rewrite the the Coriolis terms in (1) as Lagrangian derivatives. This approach may lead to an uncoupling of the motion equations and a potentially more efficient implementation of the two-time-level SLSI double Fourier method.

References

- [1] R. A. Asselin. Frequency filter for time integration. *Mon. Wea. Rev.*, 100:487–490, 1972.
- [2] J. R. Bates and A. McDonald. Multiply-upstream, semi-Lagrangian advection schemes: analysis and application to a multi-level primitive equation model. *Mon. Wea. Rev.*, 110:1831–1842, December 1982.
- [3] H.-B. Cheong. Application of double Fourier series to the shallow-water equations on a sphere. *J. Comput. Phys.*, 165:261–287, 2000. doi:10.1006/jcp.2000.6615.
- [4] H.-B. Cheong. Double Fourier series on a sphere: application to elliptic and vorticity equations. *J. Comput. Phys.*, 157:327–349, 2000. doi:10.1006/jcp.1999.6385.
- [5] J. Côté and A. Staniforth. A two-time-level semi-Lagrangian semi-implicit scheme for spectral models. *Mon. Wea. Rev.*, 116:2003–2012, October 1988.

- [6] J. Côté and A. Staniforth. An accurate and efficient finite-element global model of the shallow water equations. *Mon. Wea. Rev.*, 118:2707–2717, December 1990.
- [7] B. Haurwitz. The motion of atmospheric disturbances at the spherical earth. *J. Mar. Res.*, pages 254–267, 1940.
- [8] M. Hortal. Aspects of numerics of the ECMWF model. In *Proceedings of a seminar held at ECMWF on recent developments in numerical methods for atmospheric modeling*. European Centre for Medium-Range Weather Forecasts, 1999.
- [9] R. Jakob, J. J. Hack, and D. L. Williamson. Solutions to the shallow water test set using the spectral transform method. Technical report, National Center for Atmospheric Research, 1993. NCAR/TN-388+STR.
- [10] A. T. Layton. Cubic spline collocation method for the shallow water equations on the sphere. *J. Comput. Phys.*, 179:1–15, 2002. doi:10.1006/jcp.2002.7075.
- [11] P. E. Merilees. The pseudospectral approximation applied to the shallow water equations on the sphere. *Atmosphere*, 11(1):13–20, 1973.
- [12] S. A. Orszag. Fourier series on spheres. *Mon. Wea. Rev.*, 102:56–75, January 1974.
- [13] H. Ritchie. Application of the semi-Lagrangian method on a spectral model of the shallow water equations. *Mon. Wea. Rev.*, 116:1587–1598, 1988.
- [14] A. Robert. The integration of a low order spectral form of the primitive meteorological equations. *J. Meteor. Soc. Japan*, 44(2):237–245, 1966.

- [15] A. Robert. The integration of a spectral model of the atmosphere by the implicit method. In *Proc. of WMO/IUGG Symposium on NWP in Tokyo*, pages VII.19–VII.24. Jap. Met. Agency, 1969.
- [16] A. Robert. A semi-Lagrangian, semi-implicit numerical integration scheme for the primitive meteorological equations. *Atmos.-Ocean*, 19:35–46, 1981.
- [17] A. Robert. A stable numerical integration scheme for the primitive meteorological equations. *Atmos.-Ocean*, 19(1):35–46, 1981.
- [18] A. Robert, J. Henderson, and C. Turnbull. An implicit time integration scheme for barochlinic models of the atmosphere. *Mon. Wea. Rev.*, 100:329–335, 1972.
- [19] W. F. Spitz and P. N. Swarztrauber. A performance comparison of associated Legendre projections. *J. Comput. Phys.*, 168:330–355, 2001.
- [20] W. F. Spitz, M. A. Taylor, and P. N. Swarztrauber. Fast shallow-water equation solvers in latitude-longitude coordinates. *J. Comput. Phys.*, 145:432–444, 1998.
- [21] A. Staniforth and J. Côté. Semi-Lagrangian integration schemes for atmospheric models – a review. *Mon. Wea. Rev.*, 119:2206–2223, September 1991.
- [22] P. N. Swarztrauber. Spectral transform methods for solving the shallow-water equations on the sphere. *Mon. Wea. Rev.*, 124:730–743, April 1996.
- [23] D. L. Williamson and G. L. Browning. Comparison of grids and difference approximations for numerical weather prediction over a sphere. *J. App. Meteorol.*, 12:264–274, 1973.
- [24] D. L. Williamson, J. B. Drake, J. J. Hack, R. Jakob, and P. N. Swarztrauber. A

standard test set for numerical approximations to the shallow water equations in spherical geometry. *J. Comput. Phys.*, 102(1):211–224, September 1992.

[25] D. L. Williamson and J. G. Olson. Climate simulations with a semi-Lagrangian version of the NCAR Community Climate Model. *Mon. Wea. Rev.*, 122:1594–1610, 1993.

[26] S. Y. K. Yee. Studies on Fourier series on spheres. *Mon. Wea. Rev.*, 108:676–678, May 1980.

[27] S. Y. K. Yee. Solution of Poisson’s equation on a sphere by truncated double Fourier series. *Mon. Wea. Rev.*, 109:501–505, 1981.

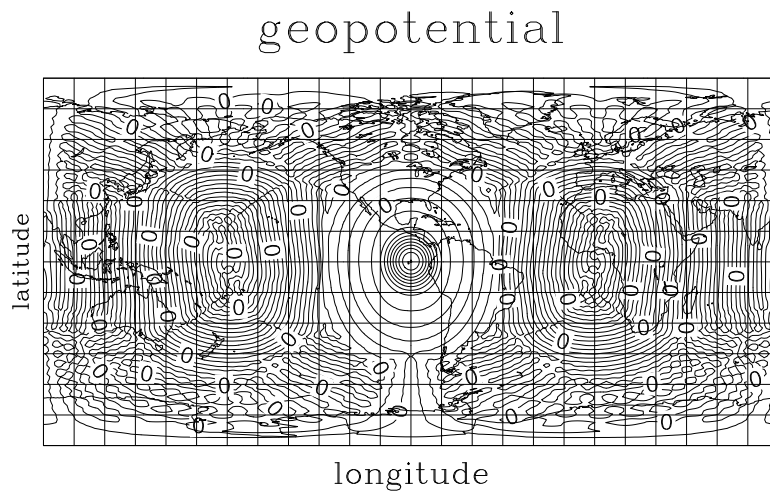


Fig. 1. Results for case 1 ($\alpha = \pi/2$): contour plot of geopotential after 12 days.

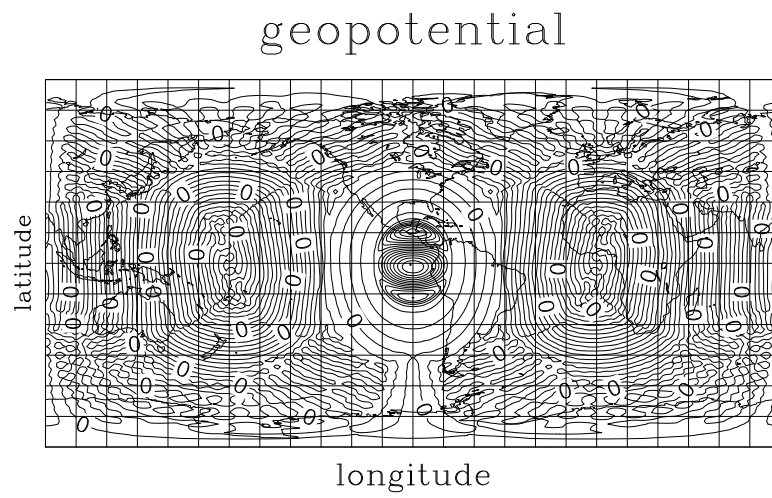


Fig. 2. Results for case 1 ($\alpha = \pi/2$): contour plot of geopotential errors after 12 days.

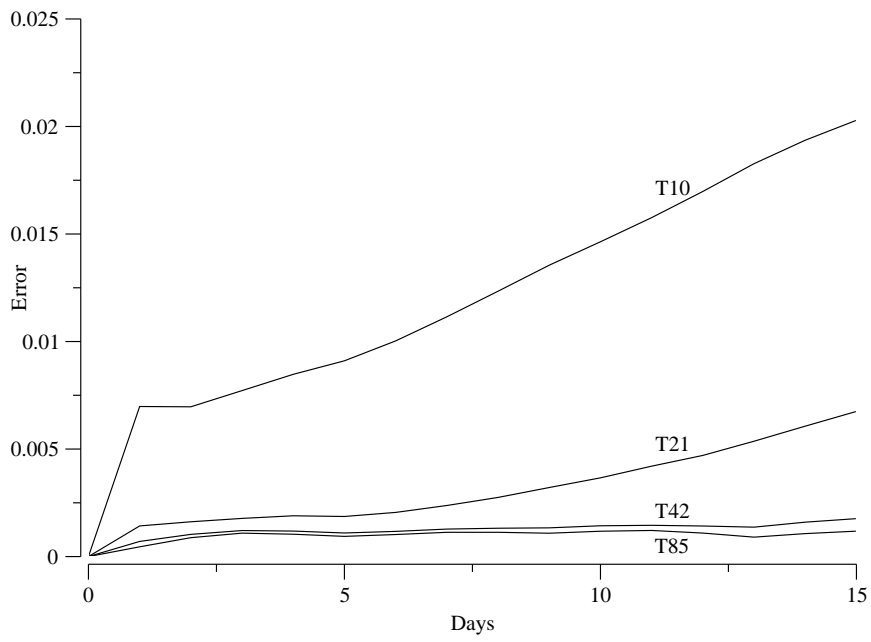


Fig. 3. Test case 5: evolution of normalized l_2 error in ϕ for 15 days.

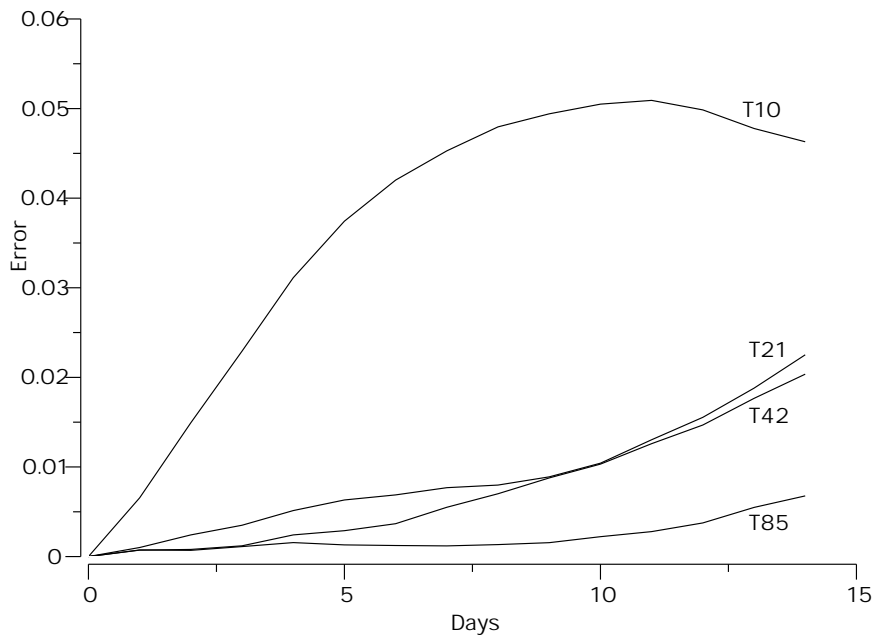
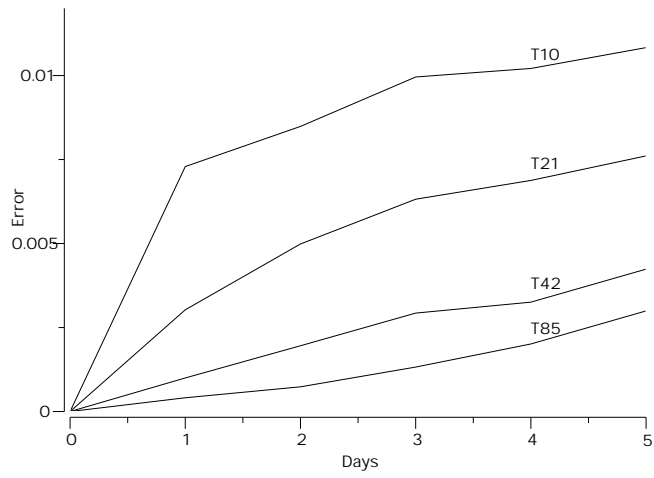
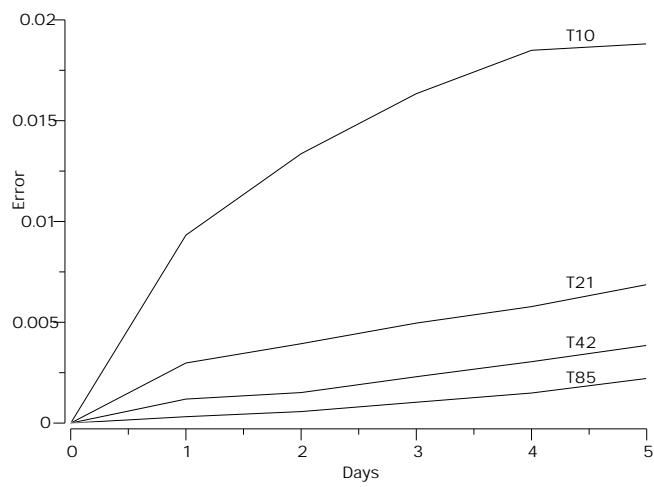


Fig. 4. Test case 6: evolution of normalized l_2 error in ϕ for 14 days.



(b)



(c)

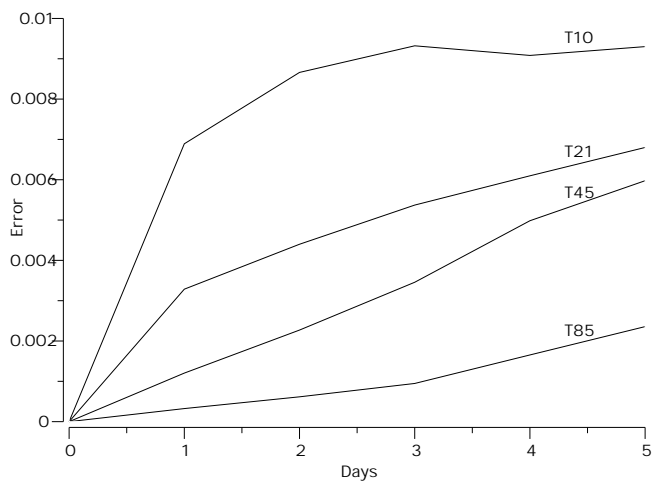


Fig. 5. Test case 7: evolution of normalized l_2 error in ϕ for 5 days in sub-cases (a),

(b), and (c).

Table 1

Convergence results. $l_2(\phi)$ = normalized l_2 error in ϕ after 5 days; p = empirical convergence rate.

Grid	Case 2 ($\alpha = \pi/2$)		Case 3 ($\alpha = \pi/3$)		Case 4 ($u_0 = 20\text{m/s}$)	
	$l_2(\phi)$	p	$l_2(\phi)$	p	$l_2(\phi)$	p
T10	1.326×10^{-3}	—	1.206×10^{-2}	—	1.149×10^{-2}	—
T21	1.670×10^{-4}	2.99	2.298×10^{-3}	2.39	2.049×10^{-3}	2.49
T42	2.133×10^{-5}	2.97	3.384×10^{-4}	2.76	2.701×10^{-4}	2.92
T85	3.766×10^{-6}	2.50	4.599×10^{-5}	2.88	5.192×10^{-5}	2.38

Table 2

Stability results with large time steps. Normalized l_2 error in ϕ is reported for each case after 5 days at resolution T85.

Δt	CFL	Case 3	Case 4	Case 7
30 min	7.59	4.130×10^{-5}	5.069×10^{-5}	2.335×10^{-3}
1 hour	15.2	4.298×10^{-5}	1.039×10^{-4}	2.740×10^{-3}
2 hours	30.4	9.948×10^{-5}	3.567×10^{-4}	unstable
3 hours	60.8	unstable	unstable	unstable

Table 3

Normalized l_2 error in ϕ for test case 3 after 5 days.

N_λ	Log formulation		Quadratic formulation	
	Linear grid	Quadratic grid	Quadratic grid	1/2-truncation
32	1.412×10^{-3}	1.407×10^{-2}	1.206×10^{-2}	2.850×10^{-2}
64	2.682×10^{-3}	2.678×10^{-3}	2.298×10^{-3}	2.906×10^{-3}
128	3.949×10^{-4}	3.944×10^{-4}	3.384×10^{-4}	3.393×10^{-4}
256	5.346×10^{-5}	5.348×10^{-5}	4.599×10^{-5}	4.603×10^{-5}